

Polarization-insensitive microwave electrometry using Rydberg atoms

Matthew Cloutman¹, Matthew Chilcott¹, Alexander Elliott², J. Susanne Otto¹, Amita B. Deb¹,³ and Niels Kjærgaard^{1,*}

¹*Department of Physics, QSO—Quantum Science Otago, and Dodd-Walls Centre for Photonic and Quantum Technologies, University of Otago, Dunedin 9016, New Zealand*

²*Department of Physics and Dodd-Walls Centre for Photonic and Quantum Technologies, University of Auckland, New Zealand*

³*School of Physics and Astronomy, University of Birmingham, Edgbaston, Birmingham B15 2TT, United Kingdom*

(Received 16 November 2023; revised 24 January 2024; accepted 25 March 2024; published 12 April 2024)

We investigate the Autler-Townes splitting for Rydberg atoms dressed with linearly polarized microwave radiation, resonant with generic $S_{1/2} \leftrightarrow P_{1/2}$ and $S_{1/2} \leftrightarrow P_{3/2}$ transitions. The splitting is probed using laser light via electromagnetically induced transparency measurements, where the transmission of probe laser light reveals a two-peak pattern. In particular, this pattern is invariant under rotation of the microwave field polarization. In consequence, we establish $S \leftrightarrow P$ Rydberg transitions as ideally suited for polarization-insensitive electrometry, contrary to recent findings [A. Chopinaud and J. D. Pritchard, Phys. Rev. Appl. **16**, 024008 (2021)].

DOI: 10.1103/PhysRevApplied.21.044025

I. INTRODUCTION

Rydberg-atom-based electric field sensors offer high sensitivities [1,2], large frequency bandwidth [3], SI-traceability, and self-calibration [4–6]. Highly excited Rydberg atoms have large transition dipole moments to nearby Rydberg states, which can be resonantly addressed with radiation in the microwave (MW) and terahertz domains. This makes Rydberg atoms responsive to a wide frequency range and their high sensitivity to electric fields is being harnessed for a growing number of applications, as for example in precision metrology [7], communication [8–11], imaging [7,12,13], and measurements of phase [14,15] and polarization [16–19].

To probe the effect of an electric field on the Rydberg atomic medium, the atoms are typically optically interrogated by two laser fields using electromagnetically induced transparency (EIT) [20]. In particular, if the applied electric field is resonant with the transition frequency between two Rydberg states, a splitting of the EIT signal emerges known as Autler-Townes (AT) splitting. The electric field strength can be directly retrieved from the AT splitting of the EIT signal [21]. In a recent study, Chopinaud and Pritchard considered optimal atomic state choices for robust microwave measurements [22]. One conclusion drawn in Ref. [22] is that the AT splitting resulting from linearly polarized microwaves driving transitions between $S_{1/2}$ and $P_{1/2}$ Rydberg levels is highly sensitive to the angle of the microwave field polarization. Furthermore,

the study, which is underpinned by experiments, claims to find a “complex AT splitting that can be used to extract a polarization ratio using an alternative method to that of [Ref. [16]],” and predicts crossings and shifting of the AT peaks.

In this paper, we show that an atom interacting with a linearly polarized microwave field gives rise to (dressed) eigenenergies with values that remain constant upon rotating the polarization. That the eigenenergies cannot change can be inferred from a symmetry argument where the quantization axis is chosen along the direction of polarization. Because of the rotational symmetry of the atomic system, no matter the orientation of the field polarization, the atom-field coupling will always be described by the same series of π -transitions. For the $S_{1/2} \leftrightarrow P_{1/2}$ transition resonantly dressed with a linearly polarized microwave field, Ref. [22] finds up to four eigenenergies, but as we show below there are only two distinct eigenenergies, each two-fold degenerate. We additionally provide an experimental demonstration that a $S_{1/2} \leftrightarrow P_{1/2}$ transition dressed by a microwave field indeed leads to two AT peaks when probed in an EIT ladder scheme. Moreover, the AT peak positions are insensitive to the rotation of the dressing field polarization.

II. POLARIZATION-INDEPENDENT EIGENENERGIES

The experiments of Ref. [22] considered cesium atoms dressed in linearly polarized microwave radiation, resonant with the transition between the two Rydberg levels

*Corresponding author: niels.kjaergaard@otago.ac.nz

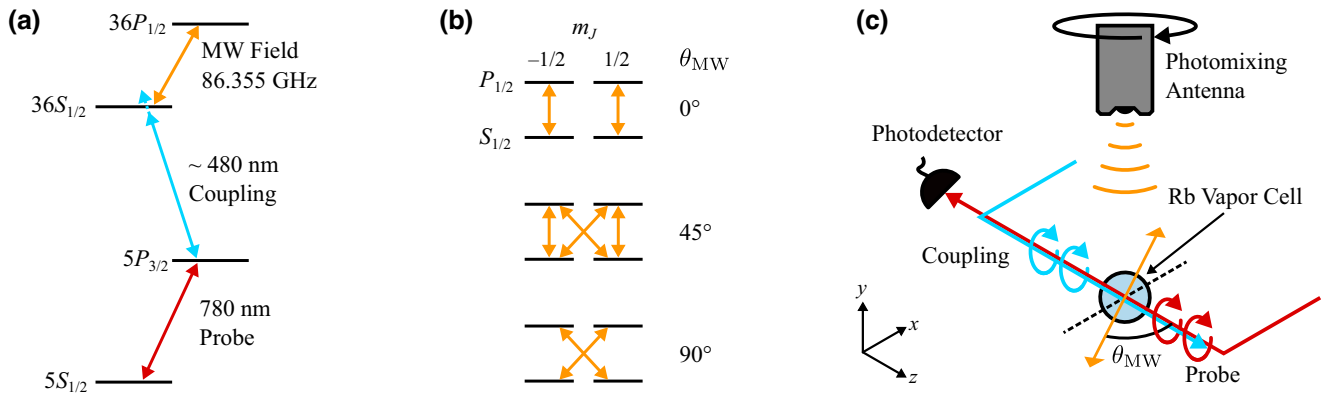


FIG. 1. (a) Reduced ⁸⁷Rb level diagram. An infrared probe laser is locked to the $5S_{1/2} \leftrightarrow 5P_{3/2}$ D2 line while a blue coupling laser scans across the $5P_{3/2} \leftrightarrow 36S_{1/2}$ transition. A microwave field couples the $36S_{1/2}$ and $36P_{1/2}$ levels separated by 86.355 GHz. (b) The m_J magnetic sublevels involved in the $36S_{1/2} \leftrightarrow 36P_{1/2}$ transition and their coupling for 0° , 45° , and 90° polarization angles. (c) Experimental setup. Probe and coupling laser beams are circularly polarized and counterpropagate through a 10-mm-diameter bubble cell filled with a rubidium vapor. The emitter is mounted in a motorized rotation stage and emits a linearly polarized field.

$65S_{1/2}$ and $65P_{1/2}$. Our experiments presented in this paper make use of the $36S_{1/2}$ and $36P_{1/2}$ levels of ⁸⁷Rb, which establishes an equivalent scenario as it is the coupled $J = 1/2 \leftrightarrow J' = 1/2$ angular momentum characteristics (factored out by the Wigner-Eckart theorem) that contain the relevant physics. Figure 1(a) shows a level diagram for ⁸⁷Rb while Fig. 1(b) shows how the $S_{1/2}$ and $P_{1/2}$ magnetic sublevels are coupled for linearly polarized MWs at angles of 0° , 45° , and 90° with respect to the quantization axis. We stress that the three situations are physically identical—the apparent difference simply results from a transformation between bases. This also means that when diagonalizing the coupling Hamiltonian one will get the same eigenvalues irrespective of the polarization angle. In the dipole and rotating-wave approximations, the coupling is $H = eE(\boldsymbol{\epsilon} \cdot \mathbf{r})/2$ for a resonant microwave field of amplitude E and polarization $\boldsymbol{\epsilon}$. Formally, performing a classical rotation R of the polarization vector $\boldsymbol{\epsilon} \rightarrow \boldsymbol{\epsilon}'$, we have $(\boldsymbol{\epsilon}' \cdot \mathbf{r}) = \mathcal{D}^\dagger(R)(\boldsymbol{\epsilon} \cdot \mathbf{r})\mathcal{D}(R)$, where $\mathcal{D}(R)$ is the quantum mechanical rotation operator [23]. Since this constitutes a similarity transformation $(\boldsymbol{\epsilon}' \cdot \mathbf{r})$ has the same eigenvalues as $(\boldsymbol{\epsilon} \cdot \mathbf{r})$. Specifically, for resonantly coupled $S_{1/2}$ and $P_{1/2}$ levels, the representation of H in the Zeeman basis with a linearly polarized microwave field oriented along the quantization axis (which we take to be the z axis) is

$$H = \frac{\hbar}{2} \begin{pmatrix} |s_{1/2}, -\frac{1}{2}\rangle & |s_{1/2}, \frac{1}{2}\rangle & |p_{1/2}, -\frac{1}{2}\rangle & |p_{1/2}, \frac{1}{2}\rangle \\ 0 & 0 & -\Omega_0 & 0 \\ 0 & 0 & 0 & \Omega_0 \\ -\Omega_0^* & 0 & 0 & 0 \\ 0 & \Omega_0^* & 0 & 0 \end{pmatrix} \begin{pmatrix} \langle s_{1/2}, -\frac{1}{2}| \\ \langle s_{1/2}, \frac{1}{2}| \\ \langle p_{1/2}, -\frac{1}{2}| \\ \langle p_{1/2}, \frac{1}{2}| \end{pmatrix}, \quad (1)$$

where the ordering of basis states $|\ell_J, m_J\rangle$ used to calculate the matrix elements $\langle \ell'_J, m'_J | \frac{1}{2}eE(\boldsymbol{\epsilon} \cdot \mathbf{r}) | \ell_J, m_J \rangle$ is shown in green at the upper and right margins of the 4×4 matrix. For example,

$$\begin{aligned} H_{13} &= \langle s_{1/2}, -\frac{1}{2} | \frac{1}{2}eE(\boldsymbol{\epsilon} \cdot \mathbf{r}) | p_{1/2}, -\frac{1}{2} \rangle \\ &= \frac{1}{2}eE \underbrace{\langle s_{1/2}, -\frac{1}{2} | r_0 | p_{1/2}, -\frac{1}{2} \rangle}_{-\left(\begin{array}{ccc} \frac{1}{2} & 1 & \frac{1}{2} \\ \frac{1}{2} & 0 & -\frac{1}{2} \end{array} \right) \langle s_{1/2} \| r \| p_{1/2} \rangle} \\ &= -eE \frac{1}{2\sqrt{6}} \langle s_{1/2} \| r \| p_{1/2} \rangle = -\frac{\hbar}{2} \Omega_0, \end{aligned} \quad (2)$$

with Rabi frequency $\Omega_0 \equiv eE \frac{1}{\sqrt{6}} \langle s_{1/2} \| r \| p_{1/2} \rangle / \hbar$. In obtaining this, the Wigner-Eckart theorem has been used to express $\langle s_{1/2}, -\frac{1}{2} | r_0 | p_{1/2}, -\frac{1}{2} \rangle$ as a signed product of a 3- j symbol and a reduced matrix element (cf. underbraced quantity). Noting that for the reduced matrix element we have $\langle s_{1/2} \| r \| p_{1/2} \rangle = \langle p_{1/2} \| r \| s_{1/2} \rangle^*$ [24], the remaining three nonzero entries of Eq. (1) follow in a similar fashion. The coupling Hamiltonian H in Eq. (1) has two eigenvalues, $\pm \hbar |\Omega_0|/2$.

Upon rotating the microwave polarization by an angle θ about the y axis, the Hamiltonian for the coupled system becomes

$$H^\theta = \frac{\hbar}{2} \begin{pmatrix} 0 & 0 & -\Omega_0 \cos \theta & \Omega_0 \sin \theta \\ 0 & 0 & \Omega_0 \sin \theta & \Omega_0 \cos \theta \\ -\Omega_0^* \cos \theta & \Omega_0^* \sin \theta & 0 & 0 \\ \Omega_0^* \sin \theta & \Omega_0^* \cos \theta & 0 & 0 \end{pmatrix}, \quad (3)$$

where, for example,

$$\begin{aligned}
 H_{13}^\theta &= \frac{1}{2}eE\langle s_{1/2}, -\frac{1}{2} | \mathcal{D}^\dagger(R)r_0\mathcal{D}(R)| p_{1/2}, -\frac{1}{2} \rangle \\
 &= \frac{1}{2}eE(\cos\theta/2\langle s_{1/2}, -\frac{1}{2} | + \sin\theta/2\langle s_{1/2}, \frac{1}{2} |) \\
 &\quad \times r_0(\cos\theta/2| p_{1/2}, -\frac{1}{2} \rangle + \sin\theta/2| p_{1/2}, \frac{1}{2} \rangle) \\
 &= \frac{1}{2}eE(\cos^2\theta/2\langle s_{1/2}, -\frac{1}{2} | r_0| p_{1/2}, -\frac{1}{2} \rangle \\
 &\quad - \underbrace{\hbar\Omega_0/eE}_{-\hbar\Omega_0/eE} \\
 &\quad + \sin^2\theta/2\langle s_{1/2}, \frac{1}{2} | r_0| p_{1/2}, \frac{1}{2} \rangle) = -\frac{\hbar}{2}\Omega_0 \cos\theta. \quad (4)
 \end{aligned}$$

Equation (3) differs from Eq. (B1) of [22] by (at least) a sign in two entries. This explains why Ref. [22] reaches the conclusion that the eigenvalues change as the polarization is rotated. In contrast, and as expected from symmetry, H^θ of Eq. (3) displays the same two eigenvalues as H in Eq. (1), namely $\pm\hbar|\Omega_0|/2$.

III. EXPERIMENT

A. $S_{1/2} \leftrightarrow P_{1/2}$ transition

To experimentally investigate the polarization dependence for an $S_{1/2} \leftrightarrow P_{1/2}$ transition probed using EIT, we perform spectroscopy via the ladder scheme of Fig. 1(a) with the experimental configuration shown in Fig. 1(c). Here, a 780-nm probe laser is locked to the $5S_{1/2}$ ($F = 2$) \leftrightarrow $5P_{3/2}$ ($F = 3$) transition in ^{87}Rb , while a 480-nm coupling laser is tuned to the $5P_{3/2} \leftrightarrow 36S_{1/2}$ transition, establishing an EIT condition for the probe beam by the atomic medium. The coupling laser is scanned, and the EIT transmission is recorded as a function of the coupling laser detuning from the $5P_{3/2} \rightarrow 36S_{1/2}$ resonance. The dashed line in Fig. 2 shows a single transmission peak, centered on zero detuning. The probe and coupling beams have Rabi frequencies of $2\pi \times 6.0$ and $2\pi \times 0.67$ MHz, respectively, and $1/e^2$ diameters of 2.0 and 1.9 mm. We modulate the amplitude of the coupling beam at 10 kHz using an optical chopper, enabling the use of lock-in detection. The probe and coupling beams counterpropagate along the z axis to suppress effects of Doppler broadening and are circularly polarized. Figure 2 shows the effect on the EIT spectrum of applying a linearly polarized MW field tuned to the $36S_{1/2} \leftrightarrow 36P_{1/2}$ transition at 86.355 GHz and propagating along the y axis [25]. Near-identical AT splitting profiles are found for the polarization angles $\theta_{\text{MW}} = 0^\circ, 45^\circ$, and 90° —corresponding to the situations of Fig. 1(b). This invariance of peak heights and splittings extends to the entire angular range of θ_{MW} . Figure 3(a) maps the AT splitting as θ_{MW} is rotated. EIT spectra are recorded every 2.5° , all showing two peaks. The peak positions remain constant within 3 MHz from their angular averages, overlaid on Fig. 3(a) as two red dashed lines split by 49 MHz.

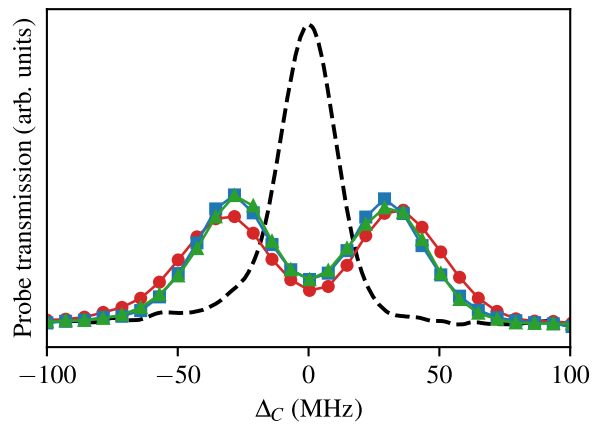


FIG. 2. Probe transmission as the coupling laser frequency is scanned. Black dashed line is the bare EIT (no MW field). Circles, squares, and triangles represent cases with a MW field oriented at $\theta_{\text{MW}} = 0^\circ, 45^\circ$, and 90° , respectively.

For a resonant MW field, this frequency splitting is related to the MW Rabi frequency Ω_{MW} by [4]

$$\Delta f = \frac{\Omega_{\text{MW}}}{2\pi}, \quad \Omega_{\text{MW}} = \frac{\mu_{ij}E}{\hbar}, \quad (5)$$

where μ_{ij} is the transition dipole moment between states $|i\rangle$ and $|j\rangle$ and E is the electric field amplitude. We attribute the small variation in the observed AT splitting to the MW field distribution not being cylindrically symmetric about the axis of rotation [26,27].

B. $S_{1/2} \leftrightarrow P_{3/2}$ transition

So far we have investigated a linear MW field dressing a $J = 1/2 \leftrightarrow J' = 1/2$ system and established that this gives rise to two eigenenergies for the coupling Hamiltonian and in turn two peaks in the EIT spectrum. Moreover, the positions and heights of these peaks remain constant as the MW polarization angle is scanned. In general, the number of unique eigenenergies for a coupled system $|J\rangle \leftrightarrow |J'\rangle$ (subject to dipole transition selection rules) can be shown to be (see Appendix A)

$$N_{\text{eig}} = \begin{cases} J + J' + 1, & 2J \text{ odd} \\ J + J' + 2, & 2J \text{ even, } J \neq J' \\ J + J' + 1, & 2J \text{ even, } J = J'. \end{cases} \quad (6)$$

We stress that the N_{eig} eigenenergies are polarization insensitive. For $J = J'$, the number of (stationary) peaks in the EIT spectrum equals N_{eig} , as for the $S_{1/2} \leftrightarrow P_{1/2}$ case considered above. For $J \neq J'$, the number of peaks will depend on which of the two the EIT coupling laser connects to (see Appendix B). If the last optical rung on the EIT ladder corresponds to the larger of J and J' , the peak number equals N_{eig} . However, if the coupling laser light

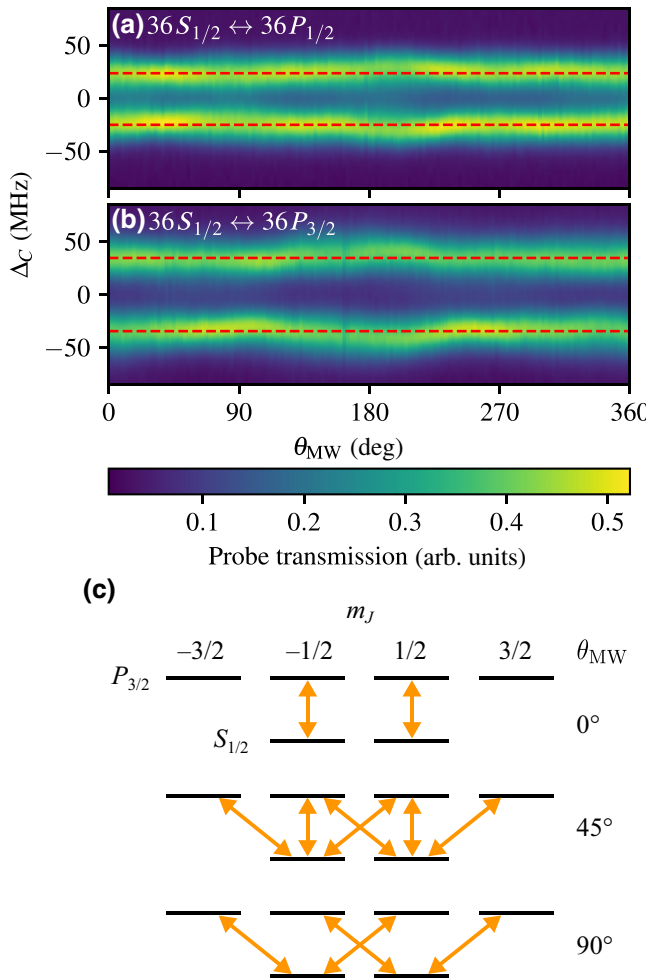


FIG. 3. Polarization scans of the (a) $36S_{1/2} \leftrightarrow 36P_{1/2}$ and (b) $36S_{1/2} \leftrightarrow 36P_{3/2}$ transitions as the coupling laser frequency is scanned. Probe transmission is normalized relative to the height of an unperturbed EIT trace; each plot is the average of 10 scans. Two Gaussians are fitted to obtain peak centers; their mean positions are plotted as red dashed lines. (c) The m_J magnetic sublevels involved in the $36S_{1/2} \leftrightarrow 36P_{3/2}$ transition, and MW couplings for $\theta_{MW} = 0^\circ, 45^\circ$, and 90° .

connects to the level with the lower of the two, the number of peaks will be $N_{\text{eig}} - 1$. Hence if for the topmost level of the ladder [Fig. 1(a)] we make use of $36P_{3/2}$ rather than $36P_{1/2}$, we would still expect only two peaks in the EIT spectrum despite the $S_{1/2} \leftrightarrow P_{3/2}$ coupling matrix having three eigenvalues. Indeed, Fig. 3(b) presents results from experimental measurements with the microwave field tuned in resonance with the $36S_{1/2} \leftrightarrow 36P_{3/2}$ transition at 88.697 GHz, revealing two peaks split by 70 MHz. This splitting is approximately 40% larger than for the $36S_{1/2} \leftrightarrow 36P_{1/2}$ transition and since the difference in transition dipole moments for the two is only approximately 2%, this must be the direct result of a change in MW power at the atoms' location [cf. Eq. (5)]. We ascribe the frequency dependence of the emitted power to the MW

source. As such, the polarization insensitivity of the $S \leftrightarrow P$ transitions of Figs. 3(a) and 3(b) makes this experimental scheme a promising candidate for measuring emitter properties.

IV. DISCUSSION AND CONCLUSION

Figure 3(c) shows how the $36S_{1/2}$ and $36P_{3/2}$ magnetic sublevels are coupled for linearly polarized MWs at angles of 0° , 45° , and 90° with respect to the quantization axis. For the 0° case it is straightforward to see that the system will have three eigenenergies, as it is represented by two independent, identical, coupled two-level systems in addition to two uncoupled energy-degenerate states, coined spectator states [28]. With the coupling laser connecting to the $S_{1/2}$ level it is clear that the spectator states will have no influence on the EIT spectrum. For the representations of the 45° and 90° cases, which both contain linkages between > 2 states, the number of eigenenergies is not obvious from inspection of the diagrams in Fig. 3(c). The Morris-Shore transformation [28] provides the Hilbert space coordinate transforms that will turn the linked systems into the unlinked one. While this method lends itself to more general polarization states [29], for the purely linearly polarized radiation considered in the present work this is simply achieved by picking a quantization axis coaxially with the polarization.

As stated above, the eigenenergies found when coupling two Rydberg levels with linearly polarized MWs are universally insensitive to the polarization angle. In turn this means that the peak positions for an EIT signal probing a level with splittings remain constant. The prominence of each (stationary) peak will, however, vary in general. The invariance of the EIT signals with angle in Figs. 3(a) and 3(b) is a special case of the coupling light connecting to a $J = 1/2$ level and the associated symmetry. Stationary eigenenergies are a necessary but not sufficient condition for the invariance, and in general the EIT signal can carry an imprint of the polarization angle, as demonstrated in Ref. [16] for a $S_{1/2} \leftrightarrow P_{3/2} \leftrightarrow D_{5/2} \leftrightarrow P_{3/2}$ ladder. In a future publication we will contrast a $S_{1/2}P_{3/2}D_{5/2}P_{3/2}$ ladder with a $S_{1/2}P_{3/2}D_{3/2}P_{1/2}$ ladder. These two scenarios display distinctly different angular EIT signatures and may form the basis of a differential polarimetry scheme for MW and terahertz radiation. Meanwhile, $S \leftrightarrow P$ Rydberg transitions, which are the focus of the present paper, can, as we have demonstrated, not be used for polarimetry. Rather, such transitions should be sought in applications where insensitivity to polarization effects is desired.

ACKNOWLEDGMENTS

This work was supported by the Marsden Fund of New Zealand (Contracts No. UOO1923 and No. UOO1729) and by MBIE (Contract No. UOOX1915). N.K. acknowledges the hospitality of Aarhus University during the write-up of

the manuscript. We thank Jevon Longdell for comments on our manuscript.

APPENDIX A: NUMBER OF COUPLING HAMILTONIAN EIGENVALUES

Here we underpin Eq. (6), which states the number of unique eigenenergies N_{eig} for a system $|J\rangle \leftrightarrow |J'\rangle$ coupled by a linearly polarized field.

The selection rules for dipole transitions imply $\Delta J = 0, \pm 1$ [30], and we first consider the case $\Delta J = 1$, so that $J' = J + 1$. Figure 4(a) shows a schematic level diagram indicating the allowed $\Delta m_J = 0$ transitions [31]. The system has a total of $4J + 4$ states that we will enumerate as indicated in Fig. 4(b). Prescribing the ordering of states using this particular enumeration, the coupling matrix becomes block diagonal [see Fig. 4(c)] with $2J + 1$

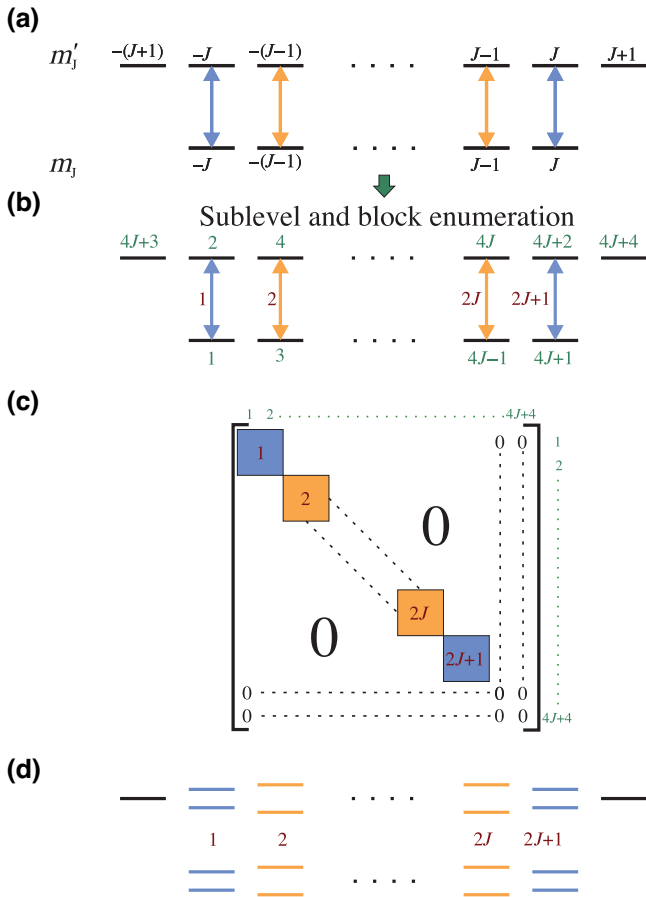


FIG. 4. (a) Magnetic sublevels m_J and m'_J for a $J \leftrightarrow J'$ transition with $J' = J + 1$, driven with a linearly polarized field; the quantization axis has been chosen along the polarization. By enumerating the sublevels (green numbers) and transitions (red numbers) as shown in (b), the coupling Hamiltonian will be represented by the block-diagonal matrix in (c). Each allowed transition $1, 2, \dots, 2J + 1$ corresponds to a 2×2 block on the diagonal of this coupling matrix. (d) Dressed state representation of the coupled $J \leftrightarrow J'$ system.

nonzero Hermitian 2×2 blocks, each corresponding to an allowed $\Delta m_J = 0$ transition designated by red numbering in Fig. 4(b). Furthermore, the coupling matrix contains one 2×2 null-matrix block arising from the stretched spectator states of the J' level. Each of the nonzero blocks is itself off-diagonal and has two nonzero eigenvalues [32]. We note the symmetry of the system [31]: transition 1 of Fig. 4(b) has the same strength as transition $2J + 1$, transition 2 has the same strength as transition $2J$, etc. This ensures that the corresponding pairs of coupling matrix blocks will share eigenvalues. Incorporating this degeneracy, the nonzero blocks amount to $2J + 1 = J + J'$ unique eigenvalues if the number of blocks is even ($2J$ odd) and $2J + 2 = J + J' + 1$ unique eigenvalues if the number of blocks is odd ($2J$ even). When including the zero eigenvalue of the null block the total number of eigenvalues becomes $J + J' + 1$ and $J + J' + 2$ [cf. Eq. (6), first and second case], respectively. These results remain valid if $\Delta J = -1$.

For $\Delta J = 0$ [33], there are $2J + 1 = J + J' + 1$ dipole-allowed transitions if $2J + 1$ is even ($2J$ odd) and hence $J + J' + 1$ unique nonzero eigenvalues, and there is no zero eigenvalue from a null block contributing to N_{eig} due to the absence of stretched spectator states. Finally, for $\Delta J = 0$ and $2J + 1$ odd ($2J$ even), there are only $2J = J + J'$ allowed transitions, because $m_J = 0 \leftrightarrow m'_J = 0$ is dipole forbidden when $J = J'$ [30]. Hence the coupling matrix will possess a zero eigenvalue in addition to the $J + J'$ nonzero eigenvalues so that $N_{\text{eig}} = J + J' + 1$ [cf. Eq. (6), third case].

APPENDIX B: NUMBER OF EIT SPECTRUM PEAKS

Figure 4(d) presents the coupled system of Figs. 4(a) and 4(b) in a dressed state picture [34]. Centered on the lower J level is a series of Autler-Townes doublets, each split by an energy equal to the difference between the two eigenvalues of the corresponding coupling block. Probing this level as the upper rung in an EIT ladder scheme would give rise to a spectrum with a number of peaks equal to $N_{\text{eig}} - 1$. The corresponding spectrum for the upper J' level would additionally include a degenerate peak from the two uncoupled, unsplit spectator states (black lines) and hence would contain N_{eig} peaks.

- [1] M. Jing, Y. Hu, J. Ma, H. Zhang, L. Zhang, L. Xiao, and S. Jia, Atomic superheterodyne receiver based on microwave-dressed Rydberg spectroscopy, *Nat. Phys.* **16**, 911 (2020).
- [2] N. Prajapati, A. K. Robinson, S. Berweger, M. T. Simons, A. B. Artusio-Glimpse, and C. L. Holloway, Enhancement of electromagnetically induced transparency based Rydberg-atom electrometry through population repumping, *Appl. Phys. Lett.* **119**, 214001 (2021).

- [3] J. Hu, H. Li, R. Song, J. Bai, Y. Jiao, J. Zhao, and S. Jia, Continuously tunable radio frequency electrometry with Rydberg atoms, *Appl. Phys. Lett.* **121**, 014002 (2022).
- [4] J. Sedlacek, A. Schwettmann, H. Kübler, R. Löw, T. Pfau, and J. Shaffer, Microwave electrometry with Rydberg atoms in a vapour cell using bright atomic resonances, *Nat. Phys.* **8**, 819 (2012).
- [5] C. L. Holloway, J. A. Gordon, S. Jefferts, A. Schwarzkopf, D. A. Anderson, S. A. Miller, N. Thaicharoen, and G. Raithel, Broadband Rydberg atom-based electric-field probe for SI-traceable, self-calibrated measurements, *IEEE Trans. Antennas Propag.* **62**, 6169 (2014).
- [6] D. A. Anderson, R. E. Sapiro, and G. Raithel, A self-calibrated SI-traceable Rydberg atom-based radio frequency electric field probe and measurement instrument, *IEEE Trans. Antennas Propag.* **69**, 5931 (2021).
- [7] C. L. Holloway, M. T. Simons, J. A. Gordon, P. F. Wilson, C. M. Cooke, D. A. Anderson, and G. Raithel, Atom-based RF electric field metrology: From self-calibrated measurements to subwavelength and near-field imaging, *IEEE Trans. Electromagn. Compat.* **59**, 717 (2017).
- [8] D. H. Meyer, K. C. Cox, F. K. Fatemi, and P. D. Kunz, Digital communication with Rydberg atoms and amplitude-modulated microwave fields, *Appl. Phys. Lett.* **112**, 211108 (2018).
- [9] Z. Song, W. Zhang, X. Liu, H. Zou, J. Zhang, Z. Jiang, and J. Qu, in *Proceedings of the 2018 IEEE Globecom Workshops (GC Wkshps)* (Abu Dhabi, United Arab Emirates, 2018), pp. 1–6.
- [10] A. B. Deb and N. Kjærgaard, Radio-over-fiber using an optical antenna based on Rydberg states of atoms, *Appl. Phys. Lett.* **112**, 211106 (2018).
- [11] J. S. Otto, M. Chilcott, A. B. Deb, and N. Kjærgaard, Distant RF field sensing with a passive Rydberg-atomic transducer, *Appl. Phys. Lett.* **123**, 144003 (2023).
- [12] L. A. Downes, A. R. MacKellar, D. J. Whiting, C. Bourgenot, C. S. Adams, and K. J. Weatherill, Full-field terahertz imaging at kilohertz frame rates using atomic vapor, *Phys. Rev. X* **10**, 011027 (2020).
- [13] D. A. Anderson, L. F. Goncalves, R. Legaie, and G. Raithel, in *Proceedings of the 2023 IEEE International Conference on Acoustics, Speech, and Signal Processing Workshops (ICASSPW)* (Rhodes Island, Greece, 2023), pp. 1–5.
- [14] D. Anderson, R. Sapiro, L. Gonçalves, R. Cardman, and G. Raithel, Optical radio-frequency phase measurement with an internal-state Rydberg atom interferometer, *Phys. Rev. Appl.* **17**, 044020 (2022).
- [15] S. Berweger, A. B. Artusio-Glimpse, A. P. Rotunno, N. Prajapati, J. D. Christesen, K. R. Moore, M. T. Simons, and C. L. Holloway, Closed-loop quantum interferometry for phase-resolved Rydberg-atom field sensing, *Phys. Rev. Appl.* **20**, 054009 (2023).
- [16] J. A. Sedlacek, A. Schwettmann, H. Kübler, and J. P. Shaffer, Atom-based vector microwave electrometry using rubidium Rydberg atoms in a vapor cell, *Phys. Rev. Lett.* **111**, 063001 (2013).
- [17] Y. Jiao, L. Hao, X. Han, S. Bai, G. Raithel, J. Zhao, and S. Jia, Atom-based radio-frequency field calibration and polarization measurement using cesium nD_J Floquet states, *Phys. Rev. Appl.* **8**, 014028 (2017).
- [18] D. A. Anderson, E. G. Paradis, and G. Raithel, A vapor-cell atomic sensor for radio-frequency field detection using a polarization-selective field enhancement resonator, *Appl. Phys. Lett.* **113**, 073501 (2018).
- [19] Y. Wang, F. Jia, J. Hao, Y. Cui, F. Zhou, X. Liu, J. Mei, Y. Yu, Y. Liu, J. Zhang, F. Xie, and Z. Zhong, Precise measurement of microwave polarization using a Rydberg atom-based mixer, *Opt. Express* **31**, 10449 (2023).
- [20] A. K. Mohapatra, T. R. Jackson, and C. S. Adams, Coherent optical detection of highly excited Rydberg states using electromagnetically induced transparency, *Phys. Rev. Lett.* **98**, 113003 (2007).
- [21] M. T. Simons, A. B. Artusio-Glimpse, A. K. Robinson, N. Prajapati, and C. L. Holloway, Rydberg atom-based sensors for radio-frequency electric field metrology, sensing, and communications, *Meas.: Sens.* **18**, 100273 (2021).
- [22] A. Chopinaud and J. Pritchard, Optimal state choice for Rydberg-atom microwave sensors, *Phys. Rev. Appl.* **16**, 024008 (2021).
- [23] J. J. Sakurai and J. Napolitano, *Modern Quantum Mechanics* (Cambridge University Press, Cambridge, 2020).
- [24] M. Auzinsh, D. Budker, and S. M. Rochester, *Optically Polarized Atoms* (Oxford University Press, Oxford, 2010).
- [25] Our experimental implementation uses a microwave field produced by a commercially available terahertz source (Toptica TeraBeam 1550), with the emitter mounted in a motorized rotation stage positioned 13 cm above the cell [cf. Fig. 1(c)].
- [26] S. Nellen, S. Lauck, G. Schwanke, M. Deumer, R. B. Kohlhaas, L. Liebermeister, M. Schell, and B. Globisch, Radiation pattern of planar optoelectronic antennas for broadband continuous-wave terahertz emission, *Opt. Express* **29**, 8244 (2021).
- [27] J. Smith, M. Naftaly, S. Nellen, and B. Globisch, Beam profile characterisation of an optoelectronic silicon lens-integrated PIN-PD emitter between 100 GHz and 1 THz, *Appl. Sci.* **11**, 465 (2021).
- [28] B. W. Shore, Two-state behavior in N -state quantum systems: The Morris-Shore transformation reviewed, *J. Mod. Opt.* **61**, 787 (2013).
- [29] G. Bevilacqua and E. Arimondo, Bright and dark Autler-Townes states in the atomic Rydberg multilevel spectroscopy, *J. Phys. B* **55**, 154001 (2022).
- [30] C. J. Foot, *Atomic Physics* (Oxford University Press, Oxford, 2005).
- [31] The strength of each transition is tied to a 3- j symbol $\begin{pmatrix} J+1 & 1 \\ m_J & 0 & -m_J \end{pmatrix} = (-1)^{J-M} [2(J+m_J+1)(J-m_J+1)/(2J+3)(2J+2)(2J+1)]^{1/2}$, with a magnitude that is symmetric in m_J and decreases monotonically with $|m_J|$ [35].
- [32] The two eigenvalues have the same the magnitude, differing by a sign, as their sum must equal the zero trace of the off-diagonal 2×2 block.
- [33] The strength of each transition when $\Delta J = 0$ is tied to a 3- j symbol $\begin{pmatrix} J & 1 & J \\ m_J & 0 & -m_J \end{pmatrix} = (-1)^{J-M-1} (M/[(2J+1)(J+1)J])^{1/2}$, with a magnitude that is symmetric in m_J and increases proportionally to $|m_J|$ [35].
- [34] C. N. Cohen-Tannoudji, in *Amazing Light* (Springer New York, 1996), p. 109.
- [35] A. R. Edmonds, *Angular Momentum in Quantum Mechanics* (Princeton University Press, Princeton, 1957).